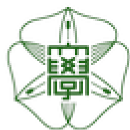

Title	Stochastic electron energy gain in inductively coupled magnetized plasmas accompanying electron reflection at chamber wall
Author(s)	Takahashi, Hironori; Nakashima, Katsuhiro; Yamamoto, Tappei; Sugawara, Hirotake
Citation	Japanese Journal of Applied Physics, 57(12), 126101 https://doi.org/10.7567/JJAP.57.126101
Issue Date	2018-10-26
Doc URL	http://hdl.handle.net/2115/75935
Rights	© 2018 The Japan Society of Applied Physics
Type	article (author version)
File Information	Takahashi-2018-JJAP-57-126101-HUSCAP.pdf

Instructions for use

Hokkaido University Collection of Scholarly and Academic Papers : HUSCAP

Stochastic electron energy gain in inductively coupled magnetized plasmas accompanying electron reflection at chamber wall *

Hironori TAKAHASHI, Katsuhiro NAKASHIMA, Tappei YAMAMOTO, and
Hirotake SUGAWARA[†]

Graduate School of Information Science and Technology, Hokkaido University, Sapporo 060-0814, Japan

Single-electron motions near the chamber wall of a type of inductively coupled magnetized plasmas were analyzed using a Monte Carlo method to understand the mechanism of electron energy gain (EEG). The analysis revealed a counterintuitive mechanism that electron reflection promotes the EEG in the presence of $\boldsymbol{E} \times \boldsymbol{B}$ drifts and collisional scattering. Distributions of EEG, energy loss, and mean electron energy were calculated using a simplified flat wall model at various strengths of electric and magnetic fields and remaining energy ratios at specular and diffuse reflections. A high stochastic EEG was observed near the wall clearly at high electric and weak magnetic fields not only in the elastic specular reflection model but also in the inelastic diffuse reflection model. An effect of boundary on the EEG mechanism was explained from the viewpoint of microscopic electron behavior.

1. Introduction

Low-pressure inductively coupled magnetized plasmas are utilized for material processing.[1–3] Among various interactions of electrons in these plasmas, deposition of electric power to electrons[4–6] is one of the most fundamental processes for plasma sustainment. A macroscopic approach to plasma power deposition was to estimate the effective power using an equivalent circuit based on a transformer model.[7] On the other hand, a detailed analysis of electron behavior revealed a structured path of loop electron current as the secondary circuit to receive electric power.[8] Understanding the power deposition mechanism via the microscopic electron behavior is essential for the physically purposeful control and design of such plasmas.

We have simulated electron motion in such magnetized plasmas.[4–6,9–11] A simulation performed for an rf plasma under confronting divergent magnetic fields showed three characteristic regions of high electron energy gain (EEG), i.e., efficient energy deposition to electrons (see Fig. 1).[12–15] The first was a region near the chamber ceiling. The electrons were accelerated by high electric fields induced by the rf antenna placed on the top of the chamber. The second was a region where a temporary ECR occurred.[5,6] Such a region, where the magnetic field

*Published source: Japanese Journal of Applied Physics, Vol. 57, No. 10, 126101-1–126101-7 (2018), DOI: 10.7567/JJAP.57.126101
†E-mail: sugawara@ist.hokudai.ac.jp

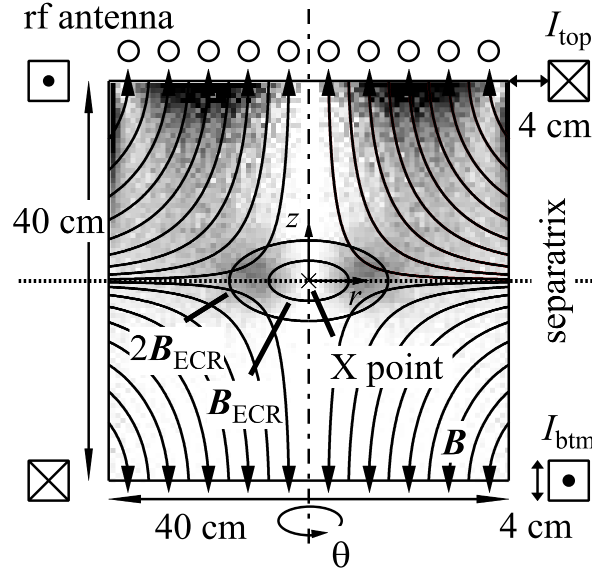

Fig. 1. Schematic of a model reactor and distribution of time-averaged net electron energy gain $G(r, z)$ in Ar at 0.67 Pa at 300 K.[12] The gray scale for $G(r, z)$ varies from white for 0 to black for 2.0 eV·rf period^{-1}·electron^{-1}. The electron reflection at the chamber wall was assumed to be elastic and specular. The dc coil currents $I_{top} = +50.0$ A and $I_{btm} = -50.0$ A; the rf antenna current $I_{rf} = 30.0$ A (amplitude). $|\boldsymbol{B}| = 0$ at the X point, and $B_{ECR} = 2\pi(m/e)f_{rf}$ ($B_{ECR} = 0.48$ mT at $f_{rf} = 13.56$ MHz).

strength satisfies the ECR condition, is located around the magnetic null point (X point) at the center of the chamber. This effect was also reported previously as partial Larmor rotation[16] or partial resonance[3] in electron motion under antiparallel gradient magnetic fields. The third was a region near the sidewall of the chamber. We suggested the possibility that electron reflection at the sidewall promoted the EEG, but details of its mechanism were left unclarified at that time.

Recently, it has been pointed out that the mechanism of EEG in the third region, which is focused on in this paper, seems to emerge in a specific configuration of electric and magnetic fields near the chamber wall.[17] Because this configuration appears in typical inductively coupled magnetized plasmas enhanced by the rf antenna placed near the chamber ceiling or sidewall, the present EEG mechanism is one of the factors to be considered in the analyses of such plasmas.

In addition, the plasma properties near the chamber wall are assumed as boundary conditions in simulations, and they sometimes govern the entire plasma structure or behavior.[18] For example, simulation and measurement of the features of electron reflection at metal sur-

faces,[19,20] measurements of the density of Ar metastable atoms near dielectric wall,[21] illustration of various electron processes at the dielectric surface,[22] and evaluations of secondary electron emission coefficient[23–25] would be informative in the discussion of practical boundary conditions. It is worthwhile to analyze the EEG mechanism in detail because it may not only contribute to plasma sustainment but may also be concerned with substantial boundary conditions.

In this paper, we analyze the effect of electron reflection on the EEG mechanism in inductively coupled magnetized plasmas on the basis of the single-electron motion observed by a Monte Carlo method adopting a simplified model. After that, we analyze the distributions of EEG, electron energy loss, and mean electron energy as functions of the distance from the wall, to investigate the stochastic effect of collisional scattering in association with the electron reflection, at various strengths of magnetic fields. The present stochastic EEG refers to the entire phenomenon that the EEG tends to be promoted by a random process of collisional scattering and has a feature that the magnetic field plays a key role, which distinguishes it from the stochastic heating induced by a plasma sheath. Furthermore, the simulations are also performed at different remaining energy ratios for reflecting electrons and for different distributions of the reflection angle as a preliminary study to establish a more realistic boundary model in the future.

2. Target system

2.1 Magnetized plasmas

The EEG mechanism near the chamber wall appears in inductively coupled magnetized plasmas, the so-called X-point plasmas and neutral loop discharge (NLD) plasmas. The X-point plasmas were originally developed as an ion source.[26–29] They are driven under confronting divergent magnetic fields applied by two coaxial coils with loop dc currents flowing in opposite directions. The plasma density is high even at low gas pressures; e.g., $\sim 10^{17}\,\mathrm{m^{-3}}$ at $\sim 1\,\mathrm{Pa}$.[27] The separatrix of the confronting divergent magnetic fields has a function to confine electrons on one side of it.[6,30] Plasma control via magnetic fields, e.g., for modulation utilizing the magnetic shutter effect for low-damage material processing and promotion of volume reactions for negative ion etchant production, is expected as a potential application of X-point plasmas.[6]

On the other hand, the NLD plasmas,[1–3,31–33] which are used for etching, are driven under a quadrupole magnetic field induced by three coaxial coils. The NLD plasma has a magnetically neutral loop, and the plasma becomes ring-shaped along the neutral loop. Its plasma density was 10^{16}–$10^{17}\,\mathrm{m^{-3}}$ at 0.067–0.13 Pa,[32,33] which is suitable for high-throughput anisotropic etching.

2.2 Geometry of cylindrical reactor and focused region

The reactor geometry (Fig. 1) assumed in this analysis was based on our preceding works.[6,12–15] The chamber was a cylinder with a diameter of 40 cm and a height of 40 cm. The magnetic field was applied by two 36-turn dc coaxial coils with their centers at $z = \pm 20.0$ cm. The top and bottom coil currents were $I_{\rm top} = +I_{\rm coil}$ and $I_{\rm btm} = -I_{\rm coil}$, respectively. The rf electric field was induced by a planar spiral antenna on top of the chamber with the current $I_{\rm antenna}(t) = -I_{\rm rf} \cos \omega t$, where $\omega = 2\pi f_{\rm rf}$ and $f_{\rm rf} = 13.56$ MHz. The antenna current was, for simplicity, approximated as concentric circular synchronous currents of $I_{\rm antenna}(t)$ flowing at $r = 2.0$, 6.0, 10.0, 14.0, and 18.0 cm and $z = 21.5$ cm. The electric field was treated to have only the azimuthal component E_θ represented as $E_\theta(r, z, t) = E_{\rm max}(r, z) \sin \omega t$. The distribution of $E_{\rm max}(r, z)$ was calculated under the given $I_{\rm antenna}$ using Faraday's law of induction. In Fig. 1, the distribution of time-averaged net EEG $G(r, z)$ in units of eV per rf period per electron is also shown, where $G(r, z)$ was calculated at $I_{\rm coil} = 50.0$ A and $I_{\rm rf} = 30.0$ A.

We focus on the region near the upper end of the sidewall, where the EEG is high and magnetic field lines run in parallel with the sidewall. This field configuration appears also between the neutral loop and the rf antenna in the NLD plasmas; i.e., in the outer region among the four regions of the quadrupole magnetic field. High EEGs in the outer region were seen also in a result of NLD plasma simulation.[4]

2.3 Hypothesis on electron motion near chamber wall

Figure 2 shows a schematic of prospected electron loci near the focused region (top view) under an rf electric field and such a dc magnetic field at which the cyclotron frequency $f_{\rm c} = eB/(2\pi m)$ is sufficiently higher than $f_{\rm rf}$, for example, $f_{\rm c} = 140.0$–419.9 MHz under $B = 5$–15 mT in the analyses demonstrated later. In this region, electrons are predicted to gain and lose energy as follows.

An electron is both accelerated and decelerated almost equally by the electric field during collisionless gyration (gyration phase). In this phase, the time-averaged EEG is almost zero, because the energy gain and loss accompanying the electron flights backward and forward relative to the direction of the electric field (i.e., toward the accelerating and decelerating directions), respectively, cancel each other. On the other hand, the electron hops always toward a specific direction (toward the $-\theta$ direction) along the wall while electron reflections at the wall occur (reflection phase). When the hopping direction matches the accelerating direction, the electron acceleration exceeds the deceleration because the part of electron locus on which the electron flight would be toward the decelerating direction is missing (acceleration phase). Likewise, after the electric field alternates, the electron deceleration exceeds because the hopping direction, which is unchanged, is toward the decelerating direction (deceleration phase).

In the presence of collisional scattering, the durations of the acceleration and deceleration

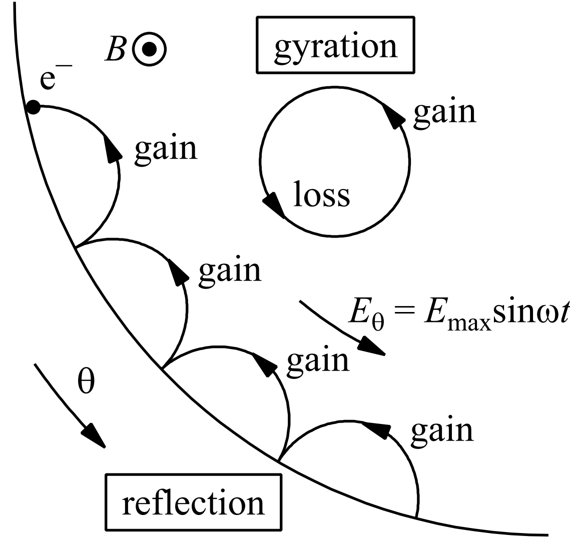

Fig. 2. Schematic of electron loci near the upper end of the sidewall of an X-point plasma reactor (top view) under rf electric and dc magnetic fields. The reflection was assumed to be elastic and specular. The time-averaged electron energy gain is almost zero during the electron gyration. That in the reflection phase is positive under the electric field depicted in the figure, but turns into negative after the electric field alternates.

phases are stochastic. It is predicted that the high EEG was observed near the wall because the acceleration in some way exceeds the deceleration in the reflection phase. The mechanism of the stochastic EEG is explained in Sect. 4.1 on the basis of simulation results.

3. Simulation model and conditions

3.1 Flat wall model

We simplify the sidewall of cylindrical chamber as a flat wall in order to investigate essential factors in the EEG mechanism. The sidewall is cut and unbent into a plane to be the yz-plane, and the distance from it is defined as x (see Fig. 3). Such a simplification has also been adopted in preceding analyses.[8,34–36]

The electric and magnetic fields (**E** and **B** fields, respectively) were defined in a Cartesian coordinate system (x, y, z) as follows:

$$\begin{aligned} \boldsymbol{E} &= (E_x, E_y, E_z) = (0, E, 0) \\ &= (0, -E_0 \sin(\omega t + \phi_0), 0) \quad (E_0 > 0,\, \omega = 2\pi f_{\rm rf}), \end{aligned} \tag{1}$$

$$\boldsymbol{B} = (B_x, B_y, B_z) = (0, 0, B) \quad (B > 0), \tag{2}$$

where the **E** and **B** fields are uniform throughout the space and ϕ_0 was basically set at $\phi_0 = 0$. In order to ensure that the EEG is independent of the initial phase of the **E** field,

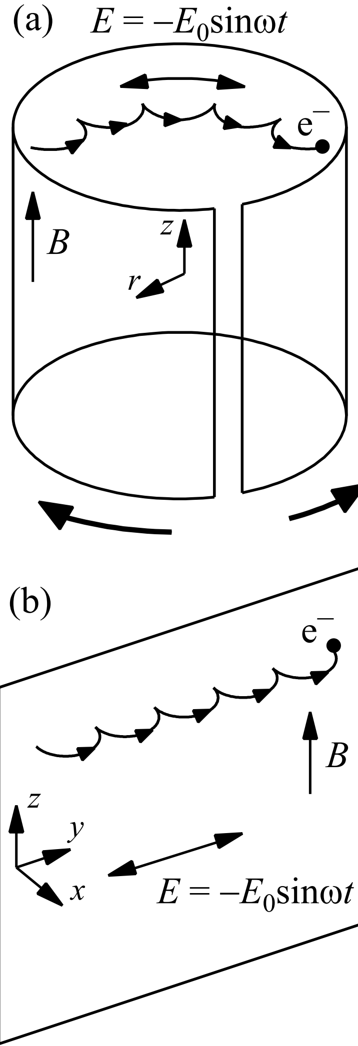

Fig. 3. Schematic of the (a) cylindrical and (b) flat wall models based on the X-point plasma reactor. $\boldsymbol{E} = (E_x, E_y, E_z) = (0, E, 0) = (0, -E_0 \sin(\omega t + \phi_0), 0)$, $\omega = 2\pi f_{\mathrm{rf}}$, $\phi_0 = 0$ or π, and $\boldsymbol{B} = (B_x, B_y, B_z) = (0, 0, B)$. The $\boldsymbol{E}$ and $\boldsymbol{B}$ fields are uniform throughout the space and $\boldsymbol{E} \perp \boldsymbol{B}$. $E_0 = 600$–$1800\,\mathrm{V\,m^{-1}}$, $f_{\mathrm{rf}} = 13.56\,\mathrm{MHz}$, and $B = 3$–$15\,\mathrm{mT}$.

the case of $\phi_0 = \pi$ was also examined. These simplified $\boldsymbol{E}$ and $\boldsymbol{B}$ fields are modelled after the focused region in the target plasmas mentioned in Sect. 2.2 and Fig. 2. Although in some of our previous simulations we considered the bias and space charge field,[5,9,37] they were not considered here to highlight the direct effect of electron reflection on the EEG mechanism.

3.2 Monte Carlo method

The electron motion in the flat wall model was simulated by a Monte Carlo method. The electron trajectory was calculated using the Runge–Kutta method for the following electron

motion equations:

$$\frac{d\boldsymbol{v}}{dt} = -\frac{e}{m}(\boldsymbol{E} + \boldsymbol{v} \times \boldsymbol{B}), \quad \frac{d\boldsymbol{r}}{dt} = \boldsymbol{v}, \tag{3}$$

where $\boldsymbol{r} = (x, y, z)$ and $\boldsymbol{v} = (v_x, v_y, v_z)$ are the position and velocity of an electron, and e and m are the electronic charge and mass, respectively. The simulation time step Δt was 3.7 ps, which is 1/20 000 of the rf period $T_{\rm rf} = 1/f_{\rm rf} = 73.7$ ns. The electron locus data were output for every $5\Delta t$.

The gas was assumed to be Ar at 0.67 Pa and 300 K. A timesaving scheme for the judgement of electron–molecule collisions[38] was adopted. The electron collision cross sections of Ar[39] include processes of elastic, excitation, and ionization collisions. Here, the electron–electron and electron–ion collisions are not considered because weakly ionized plasma is assumed. Electron reflection at the chamber wall was considered, and parameters to define it are shown in Sect. 3.4.

The initial electrons were released at $t = 0$ from the origin with velocities chosen at random from a Maxwellian distribution with a mean electron energy of 1.0 eV. Here, it is not necessary to track electrons that are sufficiently far from the wall and no longer interact with it, because the present simulation focuses on the effect of electron reflection at the wall.

We sampled the electrons after $t = 400\,T_{\rm rf}$ in order to avoid the effect of the initial condition-dependent relaxation process. We superposed the electron distributions and related quantities over the last $100\,T_{\rm rf}$ of the simulation time in order to reduce the statistical fluctuation.

3.3 Observed properties

First, we observed electron loci. Next, we calculated spatial distributions of EEG $G(x)$, electron energy loss $L(x)$, and mean electron energy $\bar{\varepsilon}(x)$. The spatial resolution was set at $\Delta x = 0.125$ mm. $G(x)$ represents the net EEG including the energy increase by acceleration and the energy decrease by deceleration during flight. When an electron moves from a sampling section to another, the accompanying energy transported by the electron is not added to $G(x)$ in both of the sampling sections. $L(x)$ represents the electron energy loss caused by inelastic collisions with gas molecules. Here, $G(x)$ and $L(x)$ are defined as the changes in electron energy per rf period per electron during its stay in a Δx. $G(x)$ and $L(x)$ are the quantities with which the power deposition and consumption of the plasma are evaluated by weighting $G(x)$ and $L(x)$, respectively, with the number of electrons in Δx.

3.4 Conditions

The parameters to determine the $\boldsymbol{E}$ and $\boldsymbol{B}$ fields for tracking electron loci were chosen as $E_0 = 600\,{\rm V\,m^{-1}}$ and $B = 16$ mT on the basis of the values calculated in the focused region in a preliminary simulation using the cylindrical model at $I_{\rm coil} = 100$ A and $I_{\rm rf} = 10$ A. Electron

loci, $G(x)$, $L(x)$, and $\bar{\varepsilon}(x)$ were also observed at $E_0 = 1000\,\mathrm{V\,m^{-1}}$ and $B = 5$–$15\,\mathrm{mT}$ for comparisons.

Actual electron interactions with the wall surface and electron behaviors in the vicinity of the wall surface are complicated; e.g., electron reflection due to the electric field of an ion sheath, ejection of secondary electrons, and detachment of adsorbed electrons from the wall. It is difficult to take them all into account owing to the lack of quantitative experimental data. However, we can consider the electron reflectivity r_{ref} and the remaining energy ratio r_{remain} at an electron reflection as the total effect of the wall surface. The current reflectivities of about 0.2–0.8 at metal surfaces were experimentally measured,[20] and they are to be included in r_{ref} and r_{remain}. Preceding works adopted, e.g., perfectly elastic reflection[40,41] ($r_{\mathrm{ref}} = r_{\mathrm{remain}} = 1.0$), partially elastic reflection[4] ($r_{\mathrm{ref}} = 0.99$ and $r_{\mathrm{remain}} = 1.0$), or perfect absorption[42] ($r_{\mathrm{ref}} = r_{\mathrm{remain}} = 0$). We take a high value of 1.0 for r_{ref} in the present simulation to clarify the direct effect of electron reflection on the EEG mechanism, although a portion of electrons may be lost at the wall practically. The r_{remain} value was varied in the range of 0.5–1.0; the reflection is elastic when $r_{\mathrm{remain}} = 1.0$; otherwise, inelastic.

r_{remain} was treated to be independent of the incident angle ϕ' and electron energy ε' for simplicity even though actual values of r_{remain} have a complicated dependence on them.[19] Here, the variables with primes represent quantities before reflection. The distribution of the reflection angle $\phi = \arctan[(v_y^2 + v_z^2)^{1/2}/v_x]$ was assumed to be of specular or diffuse reflection. Basically, specular reflection ($v_x = -v_x'$, $v_y = v_y'$, $v_z = v_z'$) was adopted in the present simulation. In addition, diffuse reflection, which is more realistic at rough surfaces, was also simulated. In the diffuse reflection model, v_x, v_y, and v_z are calculated as

$$v_x = \sqrt{r_{\mathrm{remain}}}\,|\boldsymbol{v}'|\cos\phi, \tag{4}$$

$$v_y = \sqrt{r_{\mathrm{remain}}}\,|\boldsymbol{v}'|\sin\phi\cos\psi, \tag{5}$$

$$v_z = \sqrt{r_{\mathrm{remain}}}\,|\boldsymbol{v}'|\sin\phi\sin\psi, \tag{6}$$

where $|\boldsymbol{v}'| = (v_x'^2 + v_y'^2 + v_z'^2)^{1/2}$, the reflection angle ϕ is chosen at random with a probability distribution proportional to $\cos\phi$ for $0 \le \phi < \pi/2$, and ψ is equiprobable for $0 \le \psi < 2\pi$.

4. Results and discussion

4.1 Effect of electron reflection on the electron energy gain mechanism

Figures 4 and 5 show the loci of sample electrons and the temporal variation of their energies in the flat wall model; the former shows the case of no collision during the reflection phase, and the latter shows that with some collisions.

First, a gyrating electron approached the chamber wall as induced by the $\boldsymbol{E} \times \boldsymbol{B}$ drift. Next, the acceleration phase explained in Sect. 2.3 appeared after the electron reached the wall. After the $\boldsymbol{E}$ field alternated, the deceleration phase began. Note that the $\boldsymbol{E} \times \boldsymbol{B}$ drift is

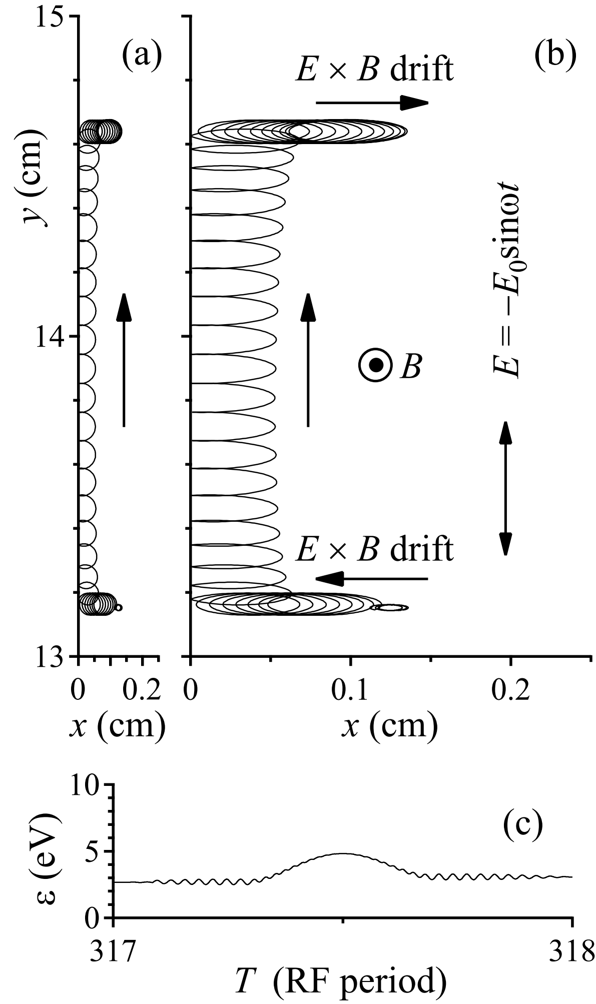

Fig. 4. Typical electron motion in the simplified flat wall model and temporal variation of electron energy: (a) sample electron locus, (b) horizontal expansion of (a) for clarification of the $\boldsymbol{E} \times \boldsymbol{B}$ drifts, and (c) electron energy. The elastic specular reflection was assumed at the wall. Ar at 0.67 Pa at 300 K. $E_0 = 600\,\mathrm{V\,m^{-1}}$, $B = 16\,\mathrm{mT}$.

directed to the $+x$ direction (leaving direction from the wall) in the latter half of an rf period, i.e., during the deceleration phase. Therefore, in this phase, electrons eventually quit from the reflection phase and restart gyration. In the cases like those shown in Fig. 4 where an electron keeps reflecting at the wall without colliding with any gas molecules, the acceleration and deceleration in the reflection phase are expected to counterbalance each other. Therefore, the total electron energy gain should be close to zero.

In the presence of collisions with gas molecules, the guiding center of an electron in the reflection phase may shift away from the wall after scattering and as a result the electron may start gyration without reflecting at the wall anymore. The point is that electrons rarely start their reflection at the wall when the $\boldsymbol{E} \times \boldsymbol{B}$ drift is toward the leaving direction. Therefore, in

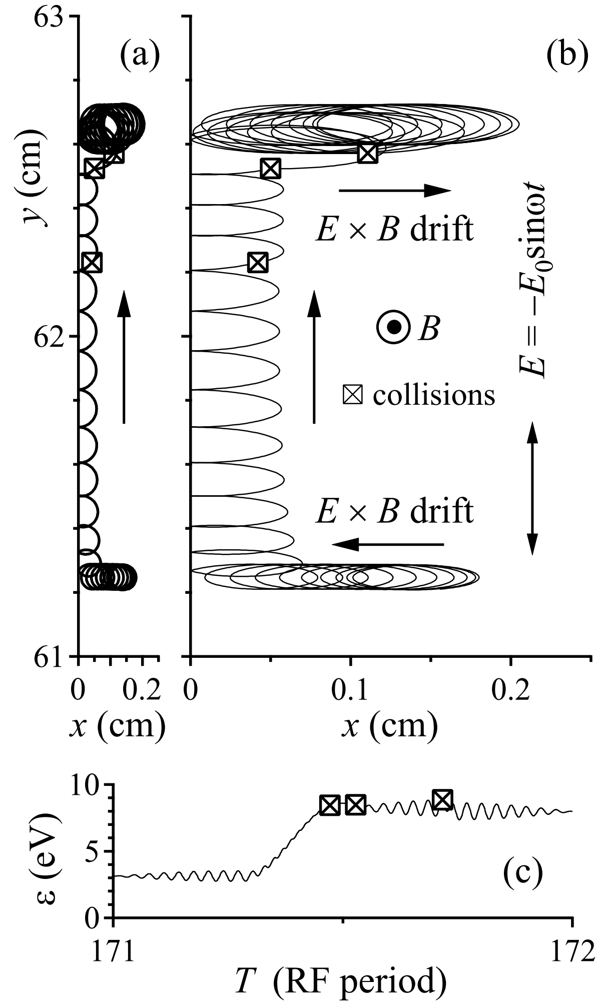

Fig. 5. (a) Typical electron motion and (b) horizontal expansion of (a), and (c) temporal variation of electron energy in the presence of collisions indicated by ⊠. The elastic specular reflection was assumed at the wall. Ar at 0.67 Pa at 300 K. $E_0 = 1000\,\mathrm{V\,m^{-1}}$, $B = 15\,\mathrm{mT}$.

most cases, the electrons start their reflection under such an $\boldsymbol{E}$ field that the $\boldsymbol{E} \times \boldsymbol{B}$ drift is toward the wall, and at that time they are in the acceleration phase. The acceleration, with which electrons start their reflection phase, can last longer than the succeeding deceleration, which can be interrupted by scattering.

Note that scattering does not always shift the guiding center away from the wall like the first collision seen in Fig. 5(a). In this case, the reflection phase continues, and it is terminated when scattering eventually shifts the guiding center away from the wall like the second collision seen in Fig. 5(a). As a result, the EEG becomes positive in total. This is the very mechanism by which electrons stochastically gain energy near the chamber wall. The mechanism can be seen when the mean free time is sufficiently longer than the cyclotron period. This requirement would be easily fulfilled in most inductively coupled magnetized

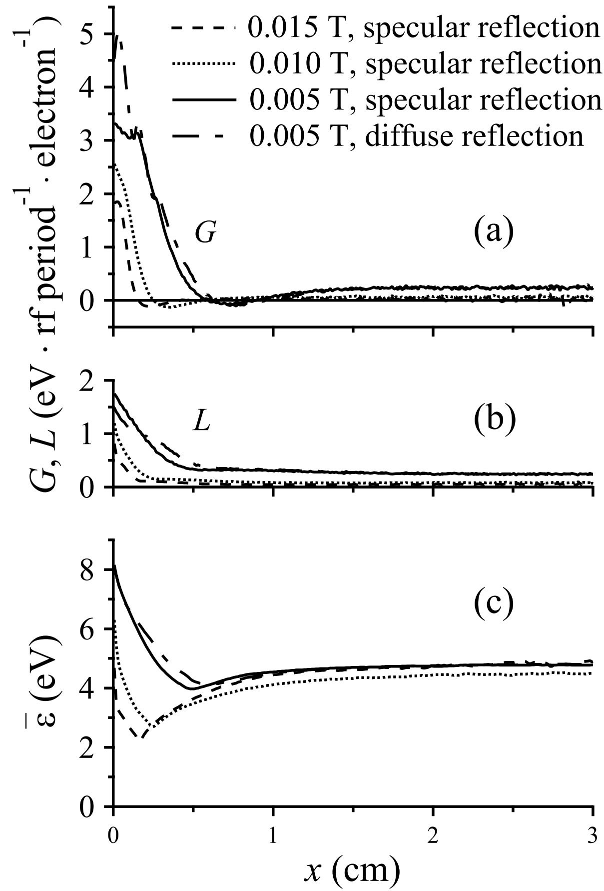

Fig. 6. Distributions of (a) electron energy gain $G(x)$, (b) electron energy loss $L(x)$, and (c) mean electron energy $\bar{\varepsilon}(x)$ under different B values and reflection conditions. x is the distance from the wall in the flat wall model. The elastic reflection was assumed. Ar at 0.67 Pa at 300 K. $E = -E_0 \sin 2\pi f_{\mathrm{rf}} t$, $E_0 = 1000\,\mathrm{V\,m^{-1}}$, and $B = 5$–$15\,\mathrm{mT}$.

plasmas where the gas pressure is low; thus, the collision frequency ν is correspondingly low; e.g., $\nu = 5$–$50 \times 10^6\,\mathrm{s^{-1}}$ and $f_{\mathrm{c}} = 140.0$–$419.9\,\mathrm{MHz}$ at $B = 5$–$15\,\mathrm{mT}$ at the gas pressure and $\boldsymbol{B}$ field assumed in the present work.

4.2 Distributions of electron energy gain, electron energy loss, and mean electron energy

Figures 6 and 7 show the distributions of the EEG $G(x)$ during flight, the electron energy loss $L(x)$ caused by collision with gas molecules, and the mean electron energy $\bar{\varepsilon}(x)$.

The $G(x)$ values near the wall were high, which is the consequence of the stochastic EEG mechanism explained in Sects. 2.3 and 4.1. This tendency became more significant under weaker $\boldsymbol{B}$ fields because the electrons flew longer distances in the acceleration direction in the acceleration phase. In addition, the region in which $G(x) > 0$ ranged farther from the wall because of the larger Larmor radius r_{L} under the weaker $\boldsymbol{B}$ fields.

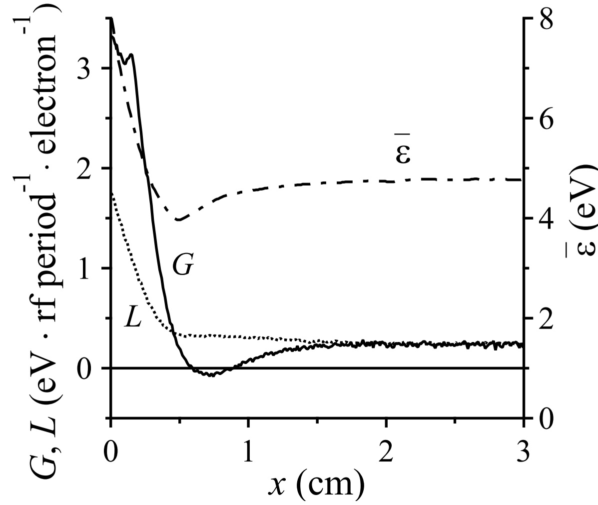

Fig. 7. Comparison of $G(x)$, $L(x)$, and $\bar{\varepsilon}(x)$ at $B = 5\,\mathrm{mT}$. The elastic specular reflection was assumed. Ar at 0.67 Pa at 300 K. $E = -E_0 \sin 2\pi f_{\mathrm{rf}} t$ and $E_0 = 1000\,\mathrm{V\,m^{-1}}$.

The $G(x)$ values were higher in the diffuse reflection model than in the specular reflection model. This is comprehensible because the ratio of the velocity components assigned for v_x tends to be high in the diffuse reflection model defined as Eqs. (4)–(6). The factor that directly contributes to $G(x)$ is v_y via a displacement in the y-direction between succeeding reflections, where v_y is a velocity component parallel to $-\boldsymbol{E}$ in the acceleration phase. However, v_x also contributes to the EEG because v_x is eventually converted into v_y during the gyration under the Lorentz force.

It is a natural result that the $L(x)$ and $\bar{\varepsilon}(x)$ values are high in the vicinity of the wall corresponding to the high $G(x)$ values there. In the region far from the wall where the effect of electron reflection was no longer seen, $G(x)$ and $L(x)$ balanced (Fig. 7), and $G(x)$, $L(x)$ and $\bar{\varepsilon}(x)$ were uniform irrespective of x. Incidentally, the primary profiles of $G(x)$, $L(x)$ and $\bar{\varepsilon}(x)$ pointed out above were observed unchanged even when the initial phase ϕ_0 of the $\boldsymbol{E}$ field was set to be not zero but π; the effect of electron reflection on the EEG mechanism is independent of ϕ_0.

4.3 Energy-resolved electron energy gain

Next, in order to analyze the factors to form $G(x)$ in Fig. 6(a), we resolved $G(x)$ by electron energy ε into $G(x, \varepsilon)$ (see Fig. 8). $G(x, \varepsilon)$ represents the energy gain per rf period by an electron having ε at x. Figure 9 shows the normalized electron energy distribution function $f(\varepsilon)$, which gives $G(x)$ as $\int_0^{\varepsilon_{\max}} G(x, \varepsilon) f(\varepsilon) d\varepsilon = G(x)$, where $\varepsilon_{\max}$ was set at 100 eV.

The $G(x, \varepsilon)$ values at low ε were low but positive across x, and those at high ε were high only near the wall. The low-ε electrons gained energy irrespective of x because their flight directions are easily turned to the accelerating direction by the instantaneous $\boldsymbol{E}$ field. On the

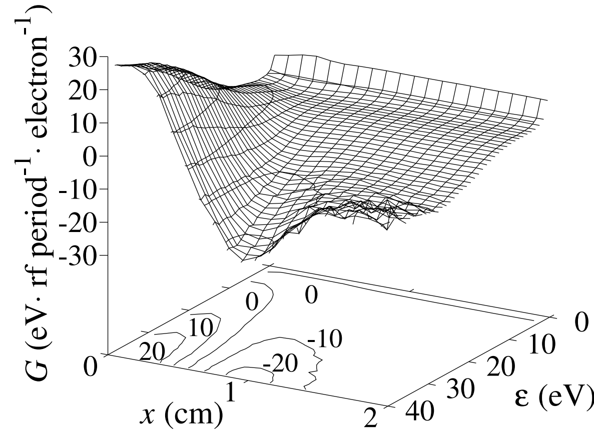

Fig. 8. Position- and energy-resolved electron energy gain $G(x, \varepsilon)$. The electron population-weighted average of $G(x, \varepsilon)$ gives $G(x)$ in Fig. 6(a). The elastic specular reflection was assumed. $E = -E_0 \sin 2\pi f_{\rm rf} t$, $E_0 = 1000\,\mathrm{V\,m^{-1}}$, and $B = 5\,\mathrm{mT}$.

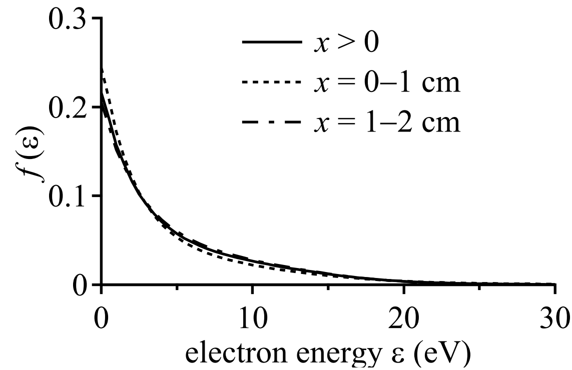

Fig. 9. Normalized electron energy distribution function $f(\varepsilon)$ in regions of $0 \leq x < 1\,\mathrm{cm}$, $1\,\mathrm{cm} \leq x < 2\,\mathrm{cm}$, and $0 \leq x$. $E = -E_0 \sin 2\pi f_{\rm rf} t$, $E_0 = 1000\,\mathrm{V\,m^{-1}}$, and $B = 5\,\mathrm{mT}$. The ratio of low-ε electrons is high under the magnetic field.

other hand, the high $G(x, \varepsilon)$ values at high ε observed near the wall are obviously due to the electron reflection. $G(x, \varepsilon)$ values near the wall increased with ε because v_y also increased with ε. Moreover, $r_{\rm L}$ reached a region far from the wall even in the reflection phase as mentioned before. Consequently, it is concluded that the positive EEG near the wall seen in Fig. 6(a) was mostly caused by the high-ε electrons.

Negative $G(x, \varepsilon)$ values were observed roughly for $x > 0.6\,\mathrm{cm}$. This energy loss is seen as

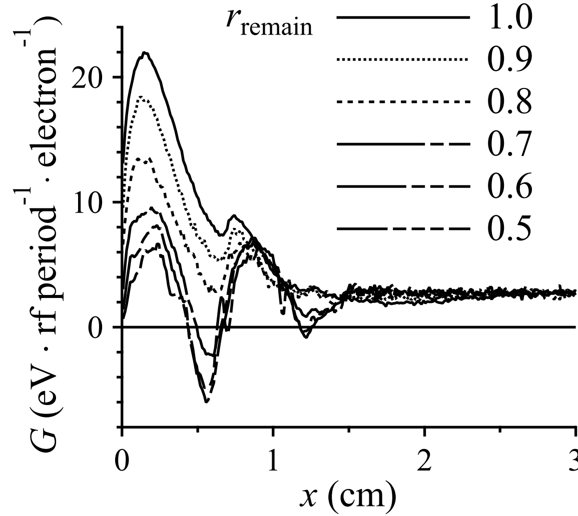

Fig. 10. Distributions of electron energy gain $G(x)$ in the diffuse reflection model. $r_{\mathrm{ref}} = 1.0$ and $r_{\mathrm{remain}} = 0.5$–$1.0$. $E = -E_0 \sin 2\pi f_{\mathrm{rf}} t$, $E_0 = 1800\,\mathrm{V\,m^{-1}}$, and $B = 3\,\mathrm{mT}$.

the negative $G(x)$ in Fig. 6(a). Its mechanism is explained in the succeeding subsection.

4.4 Energy gain under inelastic diffuse reflections

Figure 10 shows $G(x)$ distributions at $E_0 = 1800\,\mathrm{V\,m^{-1}}$ and $B = 3\,\mathrm{mT}$ under inelastic diffuse reflections at the wall. A relatively high $\boldsymbol{E}$ field and a relatively weak $\boldsymbol{B}$ field were chosen here because the energy gain during the flight in the acceleration phase was not sufficient to compensate for the energy loss by the inelastic reflection under lower $\boldsymbol{E}$ and stronger $\boldsymbol{B}$ fields in preliminary examinations.

Certainly, the effect of electron reflection weakened as r_{remain} decreased. This low r_{remain} suppressed the previously discussed contribution of the high-ε electrons to the $G(x)$ values. However, under the present high $\boldsymbol{E}$ and weak $\boldsymbol{B}$ fields, the effect was still seen in the diffuse reflection model even at $r_{\mathrm{remain}} = 0.5$.

$G(x)$ has valleys at around $x = 0.6$–$0.7\,\mathrm{cm}$. The electrons are considered to lose energy during flight in a certain x range. Figure 11 shows the $G(x, \varepsilon_{xy})$ distribution in the elastic diffuse reflection model, where $\varepsilon_{xy} = \frac{1}{2} m ({v_x}^2 + {v_y}^2)$. 500 000 electrons were tracked, and the $G(x, \varepsilon_{xy})$ values of the electrons were sampled only during the reflection phase. The $G(x, \varepsilon_{xy})$ values during the acceleration phase ($-\boldsymbol{E}$ is toward the $+y$ direction) are shown in Fig. 11(a), those during the deceleration phase ($-\boldsymbol{E}$ is toward the $-y$ direction) are in Fig. 11(b), and those throughout the rf periods are in Fig. 11(c). The number of sampled electrons for $G(x, \varepsilon_{xy})$ in Fig. 11(a) was about 1.5 times as large as that for Fig. 11(b). These numbers indicate that the acceleration phase actually lasts longer than the deceleration phase. The boundaries of the observation area where the $G(x, \varepsilon_{xy})$ values were sampled were well

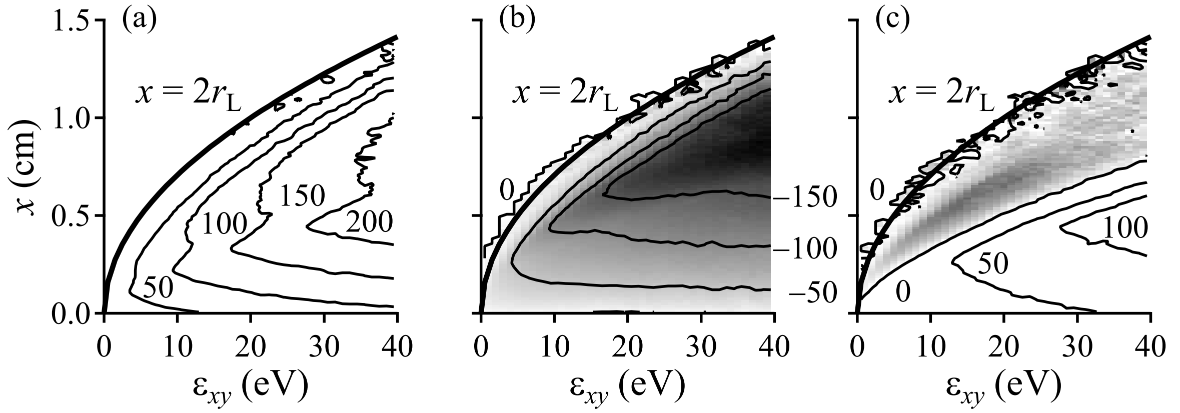

Fig. 11. Distributions of electron energy gain $G(x, \varepsilon_{xy})$ representing energy gain per rf period by an electron having ε_{xy} at x, where $\varepsilon_{xy} = \frac{1}{2}m(v_x^2 + v_y^2)$. The $G(x, \varepsilon_{xy})$ values are for the electrons in the (a) acceleration phase, (b) deceleration phase, and (c) entire rf periods. The elastic diffuse reflection was assumed. The contour step is $50\,\mathrm{eV{\cdot}rf\ period^{-1}{\cdot}electron^{-1}}$. The regions where $G(x, \varepsilon_{xy}) < 0$ are hatched with gray scales -230–$0\,\mathrm{eV{\cdot}rf\ period^{-1}{\cdot}electron^{-1}}$ for (b) and -80–$0\,\mathrm{eV{\cdot}rf\ period^{-1}{\cdot}electron^{-1}}$ for (c). $E = -E_0 \sin 2\pi f_{\mathrm{rf}} t$, $E_0 = 1800\,\mathrm{V\,m^{-1}}$, and $B = 3\,\mathrm{mT}$. Fitting curves of $x = 2r_L$ are shown together, where $r_L = \sqrt{2m\varepsilon_{xy}}/(eB)$.

curve-fitted by $x = 2r_L(\varepsilon_{xy})$ where $r_L(\varepsilon_{xy}) = m\sqrt{{v_x}^2 + {v_y}^2}/(eB) = \sqrt{2m\varepsilon_{xy}}/(eB)$, because $2r_L$ represents the electron flight range in the reflection phase.

Figure 11(a) confirms that the electron acceleration exceeds the deceleration in the acceleration phase, and Fig. 11(b) confirms that the deceleration exceeds in the deceleration phase, as predicted in Sect. 2.3. In Fig. 11(c), the $G(x, \varepsilon_{xy})$ values were positive near the wall and negative in a region far from the wall. This is because the $\boldsymbol{E} \times \boldsymbol{B}$ drift is directed toward the wall in the acceleration phase [see Fig. 12(a)], while it is directed away from the wall in the deceleration phase [see Fig. 12(b)]. In Fig. 4(b), the $\boldsymbol{E} \times \boldsymbol{B}$ drifts of the electron are seen in the reflection phase. This is how the negative $G(x, \varepsilon_{xy})$ values were localized in a certain x range. It is considered that this mechanism formed the negative $G(x, \varepsilon)$ values in Fig. 8 and the valleys in $G(x)$ in Fig. 10.

5. Conclusions

The single-electron motions near the chamber wall of an inductively coupled magnetized plasma were analyzed using a Monte Carlo method in the simplified flat wall model to understand the EEG mechanism. In general, an electron is both accelerated and decelerated almost equally by an rf $\boldsymbol{E}$ field during collisionless electron gyration (when $eB/m > 2\pi f_{\mathrm{rf}}$). The electron hops along the wall to a specific direction while electron reflections at the wall occur. When the hopping direction matches the accelerating direction, the electron acceleration ex-

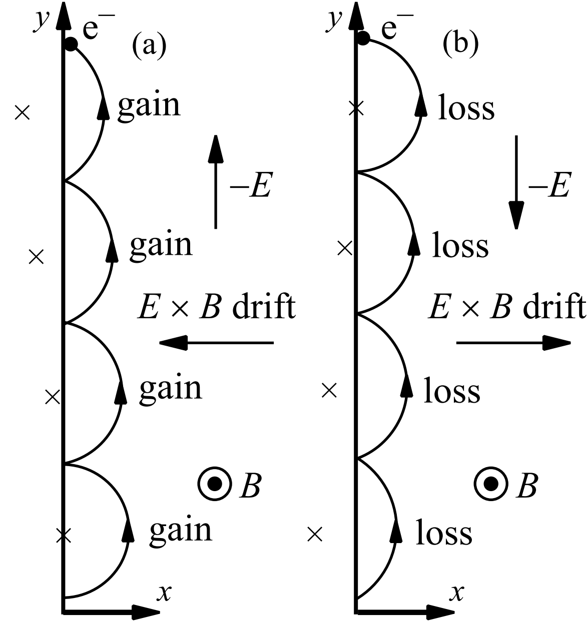

Fig. 12. Schematics of electron motion in the reflection phase: (a) acceleration phase, and (b) deceleration phase. The $\boldsymbol{E} \times \boldsymbol{B}$ drift is directed toward the wall in the acceleration phase, while it is directed away from the wall in the deceleration phase. The crosses represent the gyrocenters of drifting electrons. Actual electron orbits, e.g., those seen in Fig. 4(a), are trochoid-based curves.

ceeds the deceleration because the part of the electron locus on which the electron would be decelerated is missing. Likewise, the deceleration exceeds when the accelerating direction is missing because of electron reflection. Under such circumstances, it was revealed that the former acceleration exceeds the latter deceleration in total. This is because the reflection phase starts with the acceleration phase, during which the $\boldsymbol{E} \times \boldsymbol{B}$ drift is toward the wall. When the reflection phase is aborted by collisional scattering, the leading acceleration phase becomes longer than the following deceleration phase. The present EEG mechanism by electron reflection is different from the two conventional mechanisms in the point that the directionality of electron drift contributes to the stochastic EEG.

Next, we analyzed the distributions of the EEG $G(x)$ during flight, the electron energy loss $L(x)$ by collision, and the mean electron energy $\bar{\varepsilon}(x)$ at various combinations of E_0, B, r_{remain}, and the probability distribution function of the reflection angle ϕ in order to discuss the effect of electron reflection on the EEG mechanism. In addition, $G(x, \varepsilon)$ and $G(x, \varepsilon_{xy})$ were analyzed to better understand how $G(x)$ is formed. The following results were obtained. The EEG was high near the wall. This is the consequence of the stochastic EEG mechanism in the presence of electron reflection. This tendency was stronger and the region where $G(x) > 0$ ranged farther from the wall under the weaker $\boldsymbol{B}$ fields. $L(x)$ and $\bar{\varepsilon}(x)$ were high in the vicinity of the wall correspondingly to $G(x)$. In the region far from the wall where the effect

of electron reflection on the EEG mechanism was no longer seen, $G(x)$ and $L(x)$ balanced each other and $G(x)$, $L(x)$, and $\bar{\varepsilon}(x)$ were uniform irrespective of x. The $G(x)$ values were higher in the diffuse reflection model than in the specular reflection model. The $G(x, \varepsilon)$ values at low ε were low but positive across x, and those at high ε were high only near the wall. Although the stochastic effect weakened as r_{remain} decreased, it was still seen even under the inelastic reflection under the high $\boldsymbol{E}$ and weak $\boldsymbol{B}$ fields. In the $G(x)$ of the diffuse reflection model, valleys were observed. It was considered that the valleys were formed by the localized negative EEG in the reflection phase.

The effect of electron reflection on the EEG was seen clearly in high $\boldsymbol{E}$ and weak $\boldsymbol{B}$ fields at high r_{remain}. It is probable that this effect is involved in experimental results especially under such $\boldsymbol{E}$ and $\boldsymbol{B}$ fields that have a similar configuration to that assumed in this paper as the simplified flat wall model. In succeeding works, the model to examine the EEG mechanism would become more practical by considering the sheath electric field near the wall. Various factors besides the electron reflection at the wall may affect the EEG mechanism in the presence of the sheath. The individual effect of the electron reflection on the EEG recognized in the present paper would enable us to appropriately interpret the analysis results obtained from the model with the sheath by separating those factors. Experimental measurement of their effects, if possible, would lead to a deeper understanding of how the effect contributes to plasma sustainment.

Chamber walls are sometimes characterized as a place of electron energy loss. Therefore, it is a new qualitative finding that the chamber walls can contribute to the EEG. This interesting effect is worth considering in choosing conditions and parameters for appropriate treatments of boundaries in plasma simulations and in interpreting results of experimental and computational analyses of magnetized plasmas.

Acknowledgment

This work was supported by a KAKENHI Grant Number JP16K05626 from the Japan Society for the Promotion of Science.

References

1) W. Chen, Y. Morikawa, M. Ito, T. Hayashi, K. Sugita, H. Shindo, and T. Uchida, J. Vac. Sci. Technol. A **17**, 2546 (1999).
2) W. Chen, T. Hayashi, M. Ito, Y. Morikawa, K. Sugita, and T. Uchida, Vacuum **53**, 29 (1999).
3) T. Uchida and S. Hamaguchi, J. Phys. D **41**, 083001 (2008).
4) T. Osaga and H. Sugawara, Plasma Sources Sci. Technol. **20**, 065003 (2011).
5) Y. Minami, Y. Asami, and H. Sugawara, IEEE Trans. Plasma Sci. **42**, 2550 (2014).
6) H. Sugawara and S. Ogino, Jpn. J. Appl. Phys. **55**, 07LD05 (2016).
7) H. Tsuboi and S. Ogata, Jpn. J. Appl. Phys. **46**, 7475 (2007).
8) H. Sugawara, Jpn. J. Appl. Phys. **52**, 056101 (2013).
9) Y. Sakurai, T. Osaga, and H. Sugawara, IEEE Trans. Plasma Sci. **39**, 2550 (2011).
10) H. Sugawara, Bull. Am. Phys. Soc. **60**, 73 (2015).
11) H. Sugawara, Proc. 9th Int. Conf. Reactive Plasmas, 2015, KW2.00001.
12) K. Nakashima and H. Sugawara, Proc. Annu. Conf. Fundamentals and Materials Soc. IEE Japan, 2017, 19-E-a1-2 [in Japanese].
13) K. Nakashima and H. Sugawara, IEE Japan, 2018, PPP-18-037 [in Japanese].
14) H. Sugawara, K. Nakashima, and H. Takahashi, Proc. 20th Gaseous Electronics Meet., 2018, B-1.
15) H. Sugawara, K. Nakashima, and H. Takahashi, Proc. 24th Europhysics Conf. Atomic and Molecular Physics of Ionized Gases, 2018, P-112.
16) T. Uchida, J. Vac. Sci. Technol. A **16**, 1529 (1998).
17) H. Takahashi, H. Sugawara, K. Nakashima, and T. Yamamoto, Joint Convention Rec. Hokkaido Chapters of the Institutes of Electrical and Information Engineers, Japan, 2017, 123 [in Japanese].
18) H. Sugawara, T. Osaga, H. Tsuboi, K. Kuwahara and S. Ogata, Jpn. J. Appl. Phys. **49**, 086001 (2010)
19) H. Itoh, H. Inoue, and N. Ikuta, Denki Gakkai Ronbunshi A **110**, 363 (1990) [in Japanese].
20) T. Fujimoto, H. Itoh, T. Hayashi and N. Ikuta Denki Gakkai Ronbunshi A **115**, 1072 (1995) [in Japanese].
21) T. Sakurai, T. Kubota, Y. Takahara, Y. Inoue, and H. Hori, Jpn. J. Appl. Phys. **38**, L590 (1999).
22) Y. Golubovskii, V. Maiorov, J. Behnke, and J. F. Behnke, J. Phys. D **35**, 751 (2002).

23) A. V. Phelps and Z. Lj. Petrović, Plasma Sources Sci. Technol. **8**, R21 (1999).

24) J. Schulze, Z. Donkó, E. Schüngel, and U. Czarnetzki, Plasma Sources Sci. Technol. **20**, 045007 (2011).

25) S. Wilczek, J. Trieschmann, J. Schulze, E. Schuengel, R. P. Brinkmann, A. Derzsi, I. Korolov, Z. Donkó, and T. Mussenbrock, Plasma Sources Sci. Technol. **24**, 024002 (2015).

26) Y. Celik, T. Tsankov, and U. Czarnetzki, IEEE Trans. Plasma Sci. **39**, 2466 (2011).

27) T. Tsankov and U. Czarnetzki, IEEE Trans. Plasma Sci. **39**, 2538 (2011).

28) T. Tsankov and U. Czarnetzki, AIP Conf. Proc. **1390**, 140 (2011).

29) T. V. Tsankov, K. Toko, and U. Czarnetzki, Phys. Plasmas **19**, 123503 (2012).

30) H. Sugawara and Y. Minami, Proc. 31st Int. Conf. Phenomena in Ionized Gases, 2013, PS3-010.

31) T. Uchida, Jpn. J. Appl. Phys. **33**, L43 (1994).

32) H. Tsuboi, M. Itoh, M. Tanabe, T. Hayashi, and T. Uchida, Jpn. J. Appl. Phys. **34**, 2476 (1995).

33) H. Tsuboi, M. Itoh, T. Hayashi, and T. Uchida, Jpn. J. Appl. Phys. **36**, 6540 (1997).

34) Z. Yoshida, H. Asakura, H. Kakuno, J. Morikawa,K. Takemura, S. Takizawa, and T. Uchida, Phys. Rev. Lett. **81**, 2458 (1998).

35) H. Sugawara and Y. Sakai, J. Phys. D **41**, 135208 (2008).

36) H. Sugawara, T. Osaga, and H. Yamamoto, Plasma Sources Sci. Technol. **20**, 055002 (2011).

37) Y. Asami and H. Sugawara, IEEE Trans. Plasma Sci. **42**, 2540 (2014).

38) H. Sugawara, N. Mori, Y. Sakai, and Y. Suda, J. Comput. Phys. **223**, 298 (2007).

39) Y. Nakamura and M. Kurachi, J. Phys. D **21**, 718 (1988).

40) T. Yoshida, Y. Sakurai, H. Sugawara, and A. Murayama, Denki Gakkai Ronbunshi A **132**, 278 (2012) [in Japanese].

41) T. Yoshida, Y. Sakurai, H. Sugawara, and A. Murayama, Electr. Eng. Jpn. **185**, 9 (2013).

42) Y. M. Sung, K. Uchino, K. Muraoka, and T. Sakoda, J. Vac. Sci. Technol. A **18**, 2149 (2000).